Article:
Guo, Z., Fu, X., Zhou, R. et al. (5 more authors) (2024) A silicon-based functional self-assembled aptasensor for the detection of aflatoxin B1 by SERS sensing. Analytical Methods, 16 (41). pp. 6994-7004. ISSN: 1759-9660

https://doi.org/10.1039/d4ay01266f

Silicon-based functional self-assembled aptasensor for detection aflatoxin B1 by SERS sensing

Zhiming Guo[a, b]*, Xuan Fu[a], Ruiyun Zhou[a], Yang Zhang[a], Hesham El-Seedi[c, d], Nicholas Watson [b], Xiaobo Zou[a, d] and Megan Povey [b]

[a] *China Light Industry Key Laboratory of Food Intelligent Detection & Processing, School of Food and Biological Engineering, Jiangsu University, Zhenjiang 212013, China*

[b] *School of Food Science and Nutrition, University of Leeds, Leeds LS2 9JT, United Kingdom*

[c] *Department of Chemistry, Faculty of Science, Islamic University of Madinah, Madinah, 42351, Saudi Arabia*

[d] *International Joint Research Laboratory of Intelligent Agriculture and Agri-products Processing, Jiangsu University, Zhenjiang 212013, China*

*Corresponding author at: School of Food and Biological Engineering, Jiangsu University, Zhenjiang 212013, China. Email addressed: guozhiming@ujs.edu.cn (Z. Guo)

ABSTRACT

One of the most harmful contaminants found in corn and its products is aflatoxin B1 (AFB1), thus developing reliable detection methods is of great significance to consumers and the food industry. In this research, Au^{MBA}@Ag nanoparticles (NPs) and AgNPs deposited on a silicon wafer (Si@AgNPs) were functionalized with an aptamer and its complementary strand, respectively, and self-assembled into a SERS aptasensor, which generated strong SERS signals. AFB1 bound to aptamer prior to the complementary chain, causing Au^{MBA}@Ag NPs to detach from Si@AgNPs. The complex dissociated, leading to a decrease in signal intensity from the solid-phase substrate. Under optimal conditions, the linear detection range was 0.05-20.0 ng/mL, and the detection limit was 0.039 ng/mL. Notably, the aptasensor demonstrated a recovery rate of between 92.77% and 110.13% when utilized for the detection of AFB1 in corn flour and oil，indicating its good potential for detecting AFB1 in real sample matrices. In conclusion, a quantitative and reliable specific SERS detection system for AFB1 was developed in this study with significant applicability to food safety.

Keywords: Surface-enhanced Raman spectroscopy (SERS); Aflatoxin B1; Nanoparticles; Aptasensor; Corn

1. Introduction

Aflatoxin B1 (AFB1) is a furano-coumarin compound secreted by *Aspergillus flavus* and *A. parasiticus*. [1] Globally, AFB1 is recognized as the most toxic mycotoxin amongst the common aflatoxins (AFs). It exhibits immunosuppressive, teratogenic and carcinogenic effects, and may cause liver injury, cirrhosis and even liver and esophageal cancer. AFB1 is acknowledged by the International Agency for Research on Cancer as a Class 1 carcinogen. [2] As one of the most common cereals, corn and its products frequently encounter contamination with AFB1 throughout harvesting, storage and processing. [3] Given the elevated risk associated with AFB1, China has established strict standards, setting the maximum residue limit (MRL) of 20 μg/kg. Therefore, the development of sensitive and convenient detection methods for AFB1 is essential for the cereal industry.

At present, high performance liquid chromatography (HPLC) [4] and liquid chromatography-mass spectrometry (LC-MS/MS) [5] are the most common approaches for detecting AFB1, offering accuracy and precision. However, these methods are characterized by their operational complexity, and the need for expensive equipment. Enzyme-linked immunosorbent assay (ELISA) [6] is relatively simple to operate, but has limited specificity, and may produce false positive results. All the methods demand a level of skill and proficiency from the operators. Surface-enhanced Raman scattering (SERS) is an emerging method, which offers the advantages of easy sampling, high sensitivity and robust specificity. [7] It has the potential to address the common limitations,

making it a viable candidate for detection.

The design of the SERS substrate is a crucial factor in achieving sensitive and accurate SERS detection. Gold/silver nanoparticles are common SERS substrates due to their high local surface Plasmon resonance (LSPR), in addition to the simple preparation process and low cost. [8, 9] The signal strength of a single metal substrate is usually weak, whereas the bimetallic structure can address this issue. When the Raman reporter molecules are encapsulated within the bimetallic core-shell structure of gold and silver, they benefit from the combined effect of the superior shape and size controllability of AuNPs and the stronger Raman signal enhancement effect of AgNPs. [10] Furthermore, the metal shell serves as an effective barrier, preventing the dissociation of Raman reporter molecules, [11] resulting in high-intensity and stable Raman signals. In recent years, a variety of gold and silver bimetallic nanomaterials have been employed in SERS detection, such as Au^{ATP}@Ag nanospheres, [12] Au^{R6G}@Ag nanoflowers, [13] Au^{MBA}@Ag nanodumbbells, [14] Au^{Rh6G}@Ag nanocubes, [15] These materials all showed excellent SERS enhancement effects, which supports the aforementioned points. Among them, Au@Ag nanospheres are widely used due to their simple preparation process and prominent signal enhancement effects. [16] However, they are mostly applied in liquid systems, requiring processes such as centrifugation and resuspension before the detection. This could result in incomplete removal of free signals due to insufficient centrifugation or uneven settling of the liquid system caused by excessive centrifugation, thereby reducing the reproducibility of the results.

The silicon materials exhibit excellent stability, making them suitable as a solid-phase bearing substrate for SERS nanoenhancement materials. For example, Au@Ag NRs thin films were engineered by self-assembly at a gas-liquid interface, which were later transferred onto silicon wafer to form an Au@Ag NRs array. [17] Currently, there are various methods for fixing nanoparticles to silicon wafers, such as thermal evaporation, [18] pulsed laser deposition. [19] However, these methods often require vacuum conditions or additional energy support. Alternatively, methods like immersion plating exploit the tunability of silicon's physical and chemical properties. By using hydrofluoric acid (HF) wet etching, the morphology of silicon wafers can be altered, increasing their specific surface area and facilitating the attachment of more nanoparticles. [20] After HF modification, the silicon wafer surface is capped with hydrogen (H-terminated). Subsequently, nanoparticles are reduced by surface hydride and deposited on the silicon substrate. This method offers advantages such as self-induction, simplicity of operation, and independence from energy and vacuum conditions. While Silicon wafer has been extensively used for various nonspecific detections, but the target analyte signals may interfere with a complex matrix. This issue can be effectively resolved by utilizing nucleic acid aptamers. The aptamer is an oligonucleotide obtained through the in vitro systematic evolution of ligands by exponential enrichment (SELEX) process. The AFB1 aptamer has a stem-loop structure, which enables it to exhibit high affinity for AFB1, thereby achieving specific binding to the target. [21]

In this research, a silicon-based functionalized self-assembled solid-phase SERS aptasensor was developed for AFB1 detection. The constructed aptasensor possesses the following characteristics: (1) The Raman signal of 4-MBA embedded in the core-shell of gold and silver was enhanced effectively due to the combination of both the electromagnetic field (EF) of the nano-gap and chemical effects (CE) of the materials' various structures. (2) The specific surface area of the silicon wafer was increased by hydrofluoric acid etching, facilitating the dense deposition of AgNPs on the wafer surface. (3) The immersion plating method for depositing nanoparticles was uncomplicated and did not demand extra equipment or instruments. (4) The introduction of aptamers and complementary strands enabled AFB1 to compete with complementary strands for binding to aptamers, thus avoiding the impact of impurities and enhancing the detection sensitivity. (5) Immersion cleaning of solid-phase silicon wafer substrates was more convenient and controllable than centrifugation of liquid-phase substrates. In conclusion, this study developed a reliable and practical SERS aptasensor-based detection method for AFB1.

2. Materials and methods

2.1 Materials and reagents

Chloroauric acid ($HAuCl_4 \cdot 4H_2O$), silver nitrate standard solution ($AgNO_3$, 0.1 M), trisodium citrate ($C_6H_5Na_3O_7$, 98%), tris (2-carboxyethyl) phosphine (TCEP, 98%), hydrofluoric acid (HF, 40%) were obtained from McLean Biochemical Technology Co., Ltd (China). L-ascorbic acid (AA), acetone, sulphuric acid (H_2SO_4), hydrogen peroxide

(H_2O_2, 30%) was acquired from National medicine group chemical reagent co., ltd (China). 4-mercaptobenzoic acid (4-MBA) was purchased from Sigma-Aldrich (USA), P-type silicon wafers (ρ = 1-10 Ω·m) were bought from Puruiduo optical material co., Ltd (China). A standard solution of aflatoxin B1 (AFB1) was procured from Hua'an Magnech Bio-Tech Co., Ltd (China). All materials and reagents used were of analytical grade, no additional purification was necessary. Deionized water (DI) was used throughout the experiment. Thiol-terminal AFB1 aptamer (5'-SH-GTT GGG CAC GTG TTG TCT CTC TGT GTC TCG TGC CCT TCG CTA GGC CC-3') and thiol-terminal AFB1 complementary aptamer (5'-SH-CAG AGA GAC AAC ACG TGC CCA AC-3') were synthesized by Genscript Biotech Co., Ltd (China).

2.2 Instruments

The morphological characteristics, particle size distribution and zeta potential of nanoparticles during the preparation of Au^{MBA}@Ag NPs-Apt were investigated by transmission electron microscope (TEM) (JEM-2100, Electronics Co., Ltd., Japan) and laser particle size potentiometric analyzer (Zetasizer Lab, malvin, Anton Paar GmbH Co., Ltd., Austria). The scanning electron microscope (SEM) equipped with energy dispersive X-ray spectroscopy (SEM-EDS, Hitachi Ltd., Japan) was utilized to study the surface morphology and elemental composition. The ultraviolet-visible spectra were collected using an ultraviolet-visible spectrophotometer (UV-1601, Beijing Beifen-Ruili Analytical Instrument (Group) Co., Ltd., China). All Raman spectra were captured by automatic confocal micro-Raman imaging spectrometer (XploRA PLUS,

HORIBA Scientific Instruments Division, France), the liquid chromatography was obtained by liquid chromatograph (Shimadzu LC-20AD, Shimadzu Instruments and Equipment Co., Ltd., Japan).

2.3 Synthesis of AuNPs

AuNPs were synthesized following the procedure outlined by Yin et al. [22] Briefly, in a 250 mL beaker, 100 mL of DI was mixed with 1.6 mL of trisodium citrate (1%, W/V). Following this, the solution was brought to a boil under robust magnetic stirring at 1200 rpm before 500 μL of (2%, W/V) $HAuCl_4 \cdot 4H_2O$ was added. The solution was maintained at boiling for approximately 5 minutes and once the color transitioned from yellow to wine-red and stabilized, the procedure was stopped. The mixture was stored at 4℃ after cooling to room temperature (RT).

2.4 Synthesis of Au^{MBA}@Ag NPs

Au^{MBA}@Ag NPs were engineered according to the previously reported methods with some adjustments. [23] Under magnetic stirring, 30 μL of 4-MBA (10^{-4} M) was introduced to 3 mL of AuNPs, and after continuous stirring for 40 minutes, the surface of the AuNPs was adorned with 4-MBA. The resulting mixture underwent centrifugation at 9000 rpm for 15 minutes followed by suspension in 3 mL of DI. Following this, 60 μL of trisodium citrate (1%, W/V) and 150 μL of AA (10 mM) were added to Au^{MBA}, after stirring for 2-3 minutes, 150 μL $AgNO_3$ (10 mM) was supplemented at the rate of one drop every 15 s. During this process, the solution progressively turned from wine-red to dark orange, and the blend was stirred for an additional 30 minutes to guarantee stable nanoparticles were synthesized.

To obtain the ideal Au^{MBA}@Ag NPs, the dosages of 4-MBA were optimized by adding different final concentrations (10^{-8}, 10^{-7}, 5×10^{-7}, 10^{-6}, 5×10^{-6}, 10^{-5} M), and the thickness of the silver shell was optimized by adding different volumes (90, 120, 150, 180, 210 μL) of $AgNO_3$. The optimum amounts of both 4-MBA and $AgNO_3$ were determined according to the Raman signal intensity.

2.5 Synthesis of Si@AgNPs

Si@AgNPs were equipped by a hydrofluoric acid etching method. [24] The silicon wafers underwent a 10-minute ultrasonic cleaning in acetone followed by rinsing with DI to preliminarily eliminate soluble organic impurities. To further eradicate oxides, the silicon wafers were submerged in an H_2SO_4-H_2O_2 mixture (3:1, V/V) for 30 minutes and washed with DI. Finally, the silicon wafers were immersed in HF (5%, W/V) for 30 minutes to generate an H- terminated silicon wafer covered with Si-H bonds, [25] endowing the silicon wafer with reducibility. The silicon wafers with silicon hydrogen bonds were quickly transferred from HF to $AgNO_3$, after which the surface of the silicon wafer gradually altered from black-gray to white, indicating the construction of Si@AgNPs. The resulting silicon wafers were water-logged in a small beaker, gently shaken to remove surface impurities and then dried for later use.

In the pursuit of optimal parameters for Si@AgNPs synthesis, Si@AgNPs were manufactured using different concentrations (20, 40, 60, 80 mM) of $AgNO_3$. The optimum amount was determined by Raman characterization.

2.6 Synthesis of signal and capture probe

2.6.1 Conjugation of SH- aptamer with Au^{MBA}@Ag NPs

Equal volumes of TCEP and SH-apt were mixed and incubated for 40 minutes to activate the sulfhydryl-modified aptamers, reducing the disulfide bonds in the aptamers to monothiols. [26] The activated SH-apt was supplemented to Au^{MBA}@Ag NPs at a final concentration of 700 nM of aptamers and incubated for 12 h with shaking. To eliminate free aptamers, the mixture was redispersed in a PBS buffer after being centrifuged.

To ensure saturation in the coupling between aptamer and Au^{MBA}@Ag NPs, different final concentrations (300, 400, 500, 600, 700, 800 nM) of aptamers were studied for incubation, and the optimal concentration was identified based on the corresponding UV-Vis spectra.

2.6.2 Modification of SH-cDNA on the surface of the Si@AgNPs

SH-cDNA was activated using the same procedure as described in section 2.6.1. Si@AgNPs were incubated with complementary strands (1 μM) for 16 h, and the obtained Si@AgNPs-cDNA were gently shaken in DI to remove unbound cDNA.

2.7 Establishment of SERS aptasensor for AFB1 detection

The prepared Si@AgNPs-cDNA were immersed in the Au^{MBA}@Ag NPs solution and left to incubate for a duration of 8 h. Subsequently, they were removed and soaked in DI for 30 s to remove unbound signal probes.

To acquire SERS aptasensors with the best analytical performance, the incubation time between Au^{MBA}@Ag NPs and Si@AgNPs-cDNA was varied (4, 6, 8, 9, 10 h), and the optimal time was attained by Raman characterization.

The SERS aptasensor established under the optimum conditions were incubated with AFB1 standard solutions of different concentrations (0.05, 0.1, 0.5, 1, 5, 10, 20,

30, 40 ng/mL) for 2 h to capture AFB1. Finally, the sensors were submerged in DI water to remove the free signal probes and dried before being placed on a glass slide for Raman spectral collection. The Raman spectrometer was equipped with an excitation light source of 638 nm and a 10× objective lens, and the laser power was 30 mW. Within the wavelength range of 600-1800 cm^{-1}, each sample was collected three times with an integration time of 1 s. The collected raw spectra were preprocessed using LabSpec6 software through chemometric methods to eliminate background drift caused by fluorescence absorption. Background interference was removed by performing baseline correction through polynomial fitting, with parameters set to degree = 9 and maximum points = 82. The smoothing algorithm selected was the Polynomial method, with parameters set to factor = 10, degree = 3, and size = 12. The standard curve was established using the mean strength of Raman characteristic peak of 4-MBA at 1580 cm^{-1} and the corresponding AFB1 concentration.

2.8 Selective evaluation of sensors

Parallel experiments were conducted using other mycotoxins (ZEN, OTA, DON, FB1) commonly found in corn as interfering toxins to appraise the specificity of SERS aptasensor in AFB1 detection (all at a final concentration of 100 ng/mL). The sensors' ability to resist interference was gauged by observing the intensity change of the Raman characteristic peak.

2.9 Detection of AFB1 in real corn samples

To validate the reliability of the aptasensor, positive corn flour contaminated by AFB1, corn flour and oil artificially doped with AFB1 standard solution were prepared

as detection samples. The pretreatment process was followed according to the HPLC-post-column derivatization method in the National standard of China (GB 5009.22-2016), with slight modifications.

The equivalent volumes of gradient concentration AFB1 standard solutions were mixed with 5 g of corn flour to simulate contaminated corn tissue (positive corn flour was used as is, without the addition of standard solution). Samples were left at RT for 2 h, and then 25 mL of methanol (70%, W/V) and 1 g of NaCl were added, the mixture underwent a thorough blending using a vortex mixer for a duration of 10 minutes and then centrifuged at 6000 rpm for an additional 10 minutes. The obtained samples could be used for SERS detection now, but HPLC detection needed further purification. In this context, 10 mL of supernatant was blended with 40 mL of ultrapure water and subsequently filtered by glass fiber filter paper. Then, 25 mL of the filtrate slowly passed through the immunoaffinity column until no liquid drops remained. The immunoaffinity column was rinsed with 2×10 mL of DI, and the rapid quantitative filter paper was extended into the affinity column by gently rotating to absorb the water stains on the column wall, all the above liquids were discarded. Methanol (1 mL) was used to elute AFB1 in the immunoaffinity column, and the eluent was passed through a filter membrane (0.22 μm) for HPLC detection. In addition, 25 mL of methanol (70%, W/V) and 5 g of spiked corn oil were vortex-mixed and filtered by rapid qualitative filter paper for SERS detection. For the HPLC measurments, 10 mL of filtrate was mixed with 70 mL of ultrapure water, followed by filtration. Finally, 40 mL of filtrate was

passed through the immunoaffinity column, with subsequent operations identical to those for the corn flour samples.

Analysis was conducted using HPLC equipped with a fluorescence detector. The conditions for chromatography were as follows: chromatographic column: C18 column (150×4.6 mm×3 μm), flow rate: 0.8 mL/min, mobile phase: methanol:water (1/1, v/v), incoming sample volume: 20 μL, column temperature: 40℃, excitation wavelength: 360 nm, emission wavelength: 440 nm.

3. Results and discussion

3.1 Detection principle

The principle of AFB1 detection using silicon-based nanomaterials is shown in Fig. 1. Once a particular quantity of 4-MBA was adsorbed onto the surface of the AuNPs, the core was coated with an Ag shell, facilitating the generation of stable and intense Raman signals. These signals were then coupled with SH-apt through Ag-S bonds, creating signal probes. After the silicon wafer was etched by HF, the surface was covered with Si-H bonds to promote the deposition of AgNPs, and SH-cDNA was later coupled with Si@AgNPs through Ag-S bonds. The generated aptasensor exhibited a robust Raman signal since Au^{MBA}@Ag NPs-Apt was combined with Si@AgNPs-cDNA in accordance with the principle of base complementary pairing. By virtue of its high affinity for AFB1, aptamer preferentially bonds to it, causing the release of signal probes from Si@AgNPs-cDNA. [27] Consequently, the Raman signal intensity from the silicon wafer is diminished, leading to negative correlation between the signal intensity of SERS aptasensor and the concentration of AFB1.

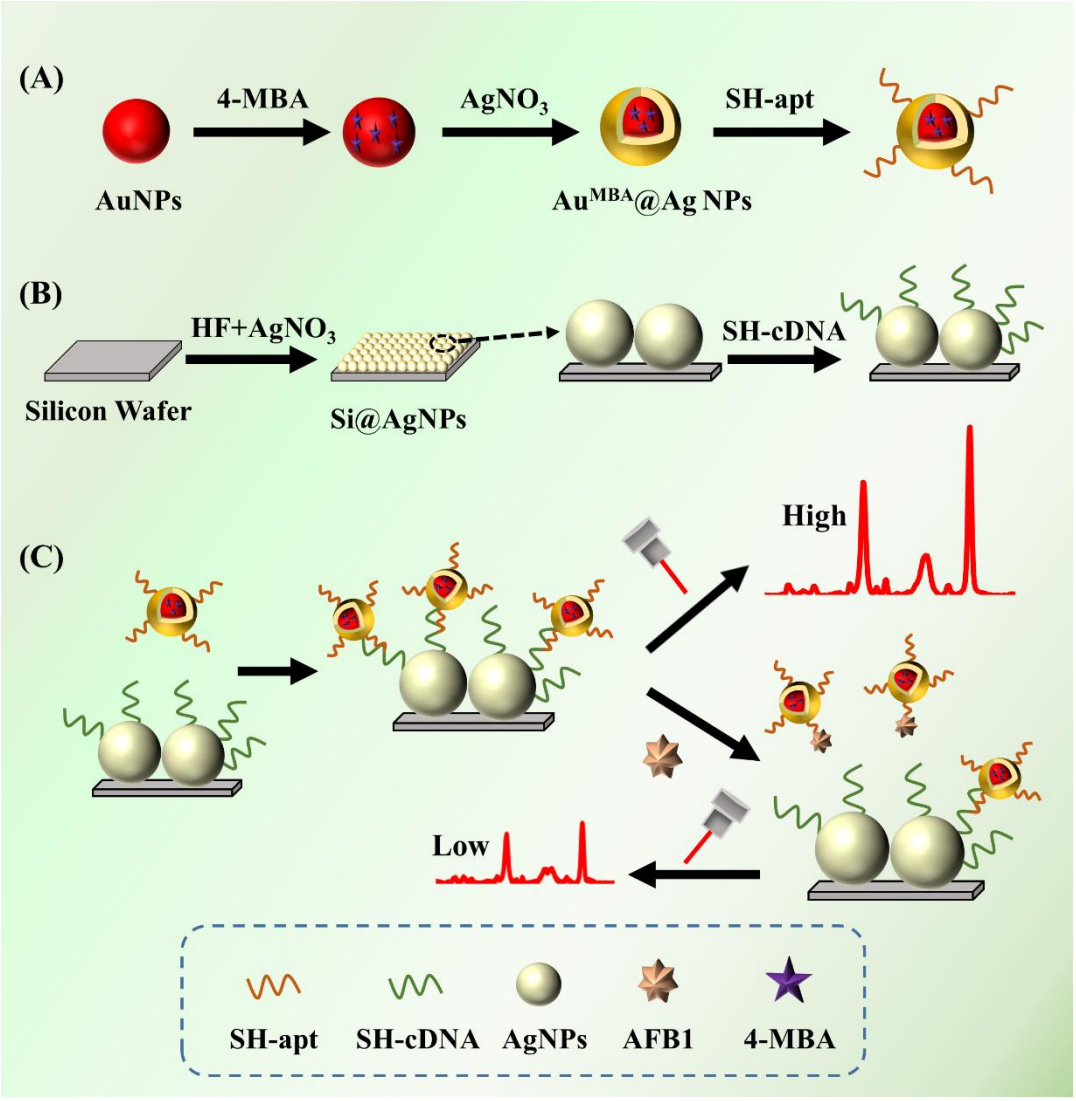

Fig. 1 Schematic diagram of SERS aptasensor for AFB1 detection. (A) Preparation of Au^{MBA}@Ag NPs-Apt, (B) Preparation of Si@AgNPs-cDNA, (C) Detection of AFB1.

3.2 Characterization and optimization of Au^{MBA}@AgNPs-Apt

3.2.1 Characterization of Au^{MBA}@Ag NPs-Apt

TEM and particle size distribution DLS images (Fig. 2A-B) revealed that the AuNPs were well-dispersed with a mean diameter of 20.99 nm. Upon coating with the Ag shell, the nanoparticles were aggregated to some extent, and an Ag layer can be observed outside the Au core (Fig. 2D), with an average diameter of 29.79 nm (Fig. 2E), in which the thickness of the Ag shell was about 4.4 nm. Significantly, compared with

AuNPs, the UV absorption peak at 530 nm underwent a blue-shift to 487 nm, in addition to a new absorption peak materializing at 403 nm, which corresponded to the LSPR of the gold nucleus and the silver shell, respectively (Fig. 2C), confirming the combination of the Ag shell with Au nucleus. Aptamer's absorption peak emerged at 262 nm following its incubation with Au^{MBA}@Ag NPs (Fig. 2F), proving the efficacious coupling between the two materials.

The alterations in potential throughout the signal probe synthesis are depicted in Fig. 2G. Given that AuNPs were synthesized using the trisodium citrate reduction method, they had a significant number of citric acid electrons on the surface, thus the nanoparticles were negatively charged, and the potential of the Au@Ag NPs slightly rose compared to the AuNPs. Further, the negative potential exhibited by the aptamer was attributed to the phosphoric acid residues, [28] and although the nanoparticle solution maintained a negative value throughout the preparation process, the specific absolute values differed. The Zeta potential absolute value of the nucleic acid aptamer was lower than that of Au@AgNPs. Therefore, after the nucleic acid aptamer successfully coupled with Au@AgNPs, it neutralized the original potential, resulting in a decrease in the absolute value of the composite's potential (i.e., an increase in potential). The color change that occurred during distinct stages of signal probe synthesis is shown in Fig. 2H, where both 4-MBA and aptamers did not induce any noticeable change in the color of the Au@Ag NPs, whereas the coating of Ag shell transformed the nanoparticles from wine-red to dark orange. In terms of Raman signals, AuNPs itself had no Raman signal,

and the Raman signal of 4-MBA was exceedingly faint. Upon the adsorption of 4-MBA onto AuNPs, the Raman signal exhibited a modest rise, and spiked significantly when the nanoparticles were encased in Ag shells (Fig. 2I). This demonstrated the synergistic reinforcement effect of the bimetallic core-shell structure, which was consistent with previously reported results. [29] Further, the characteristic peak of 4-MBA at 1580 cm^{-1} was used in the subsequent detection and analysis as it showed the highest intensity during measurement.

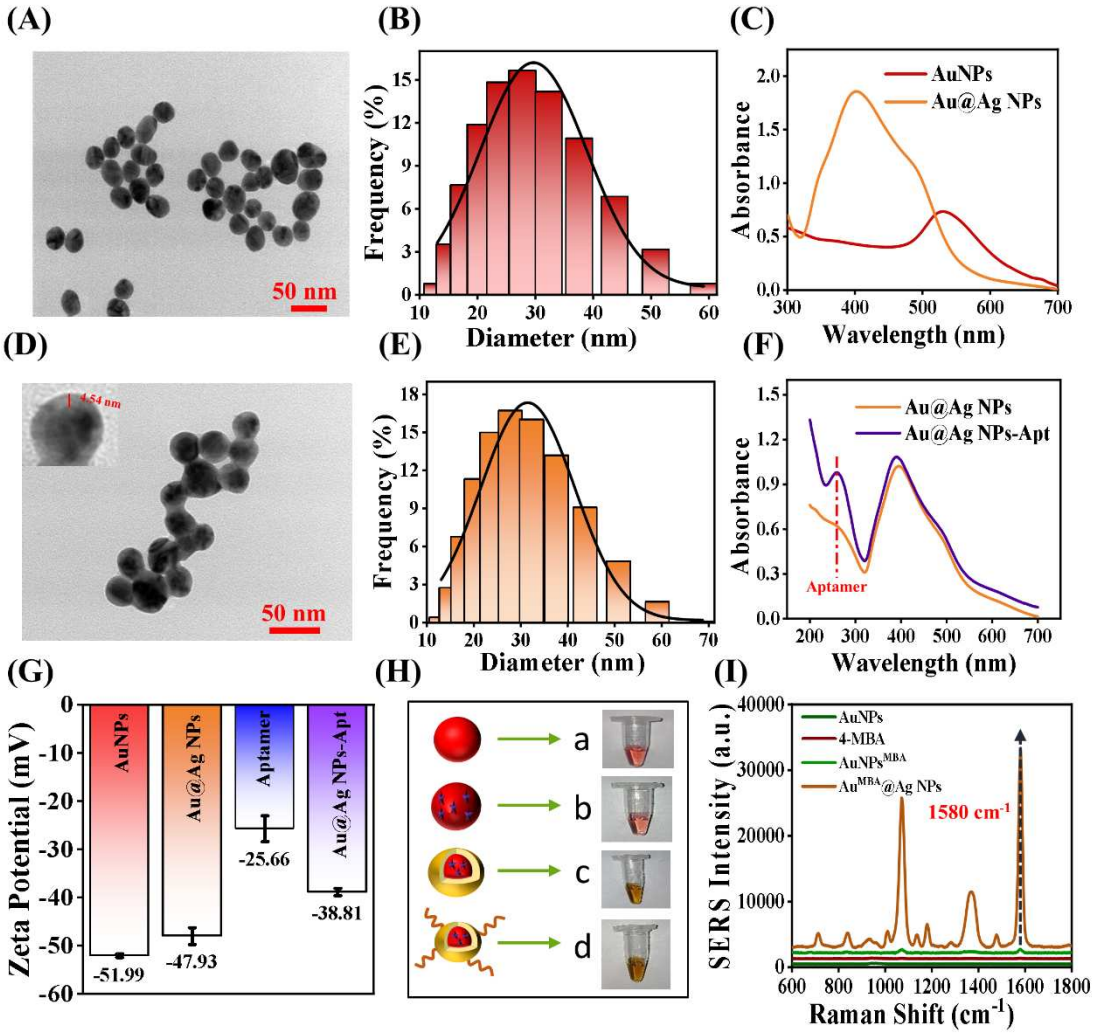

Fig. 2 (A) TEM image of AuNPs, (B) Particle size distribution from DLS results of AuNPs, (C) UV-vis spectra of AuNPs and Au@Ag NPs, (D) TEM image of Au@Ag

NPs, (E) Particle size distribution from DLS results of Au@Ag NPs, (F) UV-vis spectra of Au@Ag NPs and Au@Ag NPs-Apt, (G) Zeta potential changes during the synthesis of signal probe, (H) Color changes during the synthesis of signal probes, (I) Raman spectra of AuNPs, $AuNPs^{MBA}$, Au^{MBA}@Ag NPs.

3.2.2 Optimization of Au^{MBA}@Ag NPs-Apt

The alteration of the UV-vis spectra for signal probes synthesized with various volumes of $AgNO_3$ is illustrated in Fig. 3A. With the augmentation of the silver shell thickness, the UV absorption peak of AuNPs exhibited a blue-shift and subsequent attenuation until it was entirely obscured. Simultaneously, the peak associated with AgNPs was red-shifted and enhanced, and the solution progressively darkened in color and became turbid. The synthesized Au^{MBA}@Ag NPs displayed respective average sizes of 25.88, 27.63, 29.79, 32.44 and 35.00 nm, respectively. A substantial aggregation of the nanoparticles and a reduction in the uniformity of particle size distribution were observed when the quantity of $AgNO_3$ added was ≥ 180 μL (Fig. S1).

Raman spectra were utilized to ascertain the optimal amount of $AgNO_3$ and 4-MBA. The SERS intensity of Au^{MBA}@Ag NPs displayed a progressive rise as the volume of $AgNO_3$ expanded (90-150 μL). However, the signal began to decrease when the volume of $AgNO_3$ reached 180 μL (Fig. 3B). This decline in intensity was attributed to the shielding effect of an excessively thick silver shell on the 4-MBA signal. [30] Therefore, 150 μL of $AgNO_3$ was selected as the optimal dosage. The SERS intensity of Au^{MBA}@Ag NPs exhibited an ongoing progress with the increase of 4-MBA (Fig. S2).

However, variability among the spectra also altered as evident by the increase in error bar (Fig. 3C). The variability was significantly higher when the concentration was ≥ 5×10^{-6} M (RSD > 10%), aligning with the observation that excessive 4-MBA leads to the aggregation of AuNPs. [31] To guarantee the consistency and stability of the subsequent SERS aptasensor, 1×10^{-6} M of 4-MBA was selected to combine with AgNPs.

The changes in the UV absorption peak of Au^{MBA}@Ag NPs after incubation with aptamers (300 to 800 nM) are shown in Fig. 3D. The findings suggest that the coupling between Au^{MBA}@Ag NPs and aptamers reached saturation at 700 nM, which was selected as the optimum concentration.

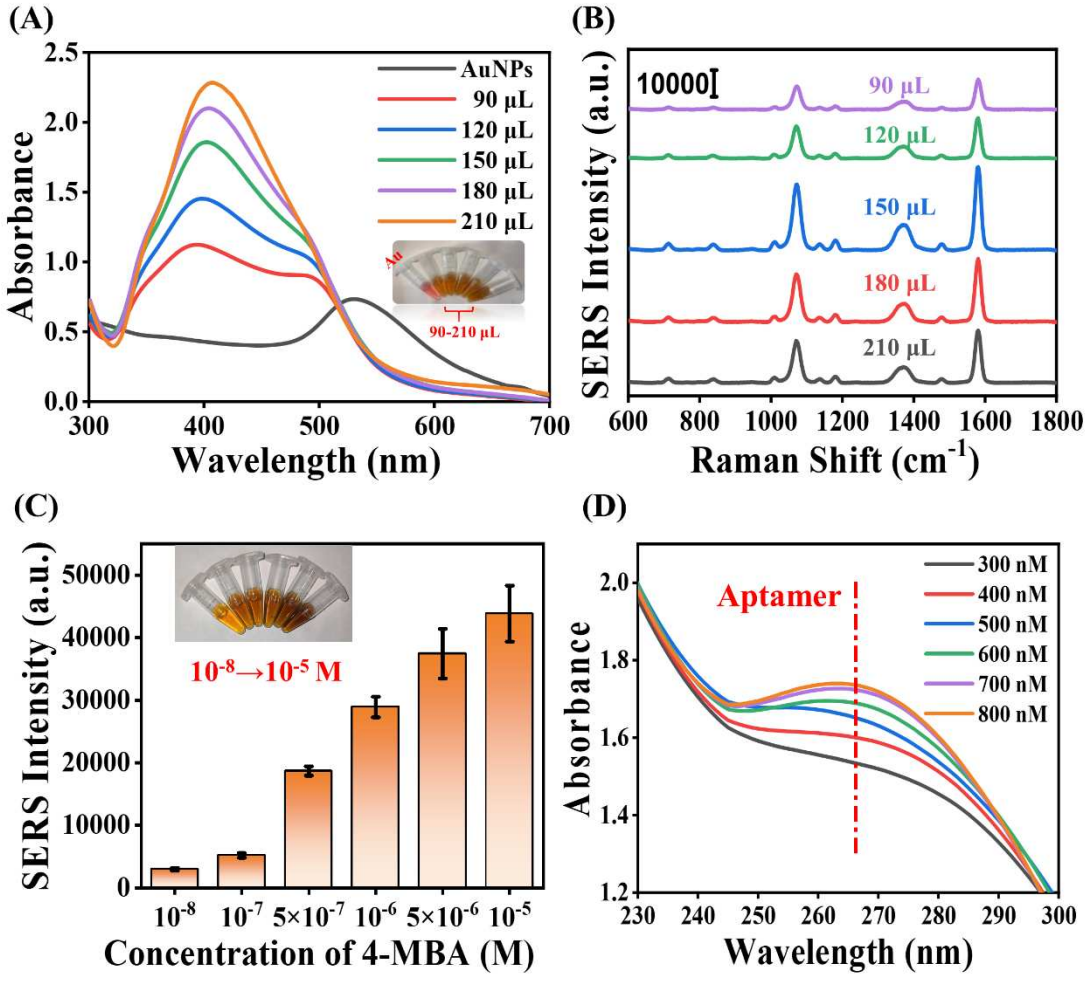

Fig. 3 (A) UV-Vis spectra of AuNPs/Au^{MBA}@Ag NPs with different silver shell thicknesses, (B) The effect of $AgNO_3$ amount on SERS intensity of Au^{MBA}@Ag NPs and the corresponding physical pictures, (C) The effect of 4-MBA amount on SERS intensity of Au^{MBA}@Ag NPs and the corresponding physical pictures, (D) UV-Vis spectra of signal probe with different concentrations of aptamer.

3.3 Characterization and optimization of Si@AgNPs-cDNA

The impact of $AgNO_3$ concentration on the morphological features and SERS intensity of the Si@AgNPs are presented in Fig. 4A and Fig. 4B, respectively. When the concentration of $AgNO_3$ was low (Fig. 4A(a)), tiny, sparsely distributed AgNPs on the silicon wafer led to weak Raman signals. This phenomenon can be attributed to the formation mechanism of AgNPs, which can be divided into three stages: induction, nucleation and growth. [32] During the reaction, Ag^+ undergoes initial reduction to Ag, leading to the formation of silver agglomerates and AgNPs are generated after reaching the nucleation concentration. The low concentration of $AgNO_3$ resulted in a slow growth rate of crystal nuclei, preventing the formation of many uniform AgNPs. Too large a gap between adjacent AgNPs cannot produce large electromagnetic enhancement under laser excitation. When the concentration of silver nitrate climbed to 40 mM (Fig. 4A(b)), the diameter of nanoparticles increased, resulting in more spherical and densely distributed nanoparticles. As a result, the SERS signal was also effectively enhanced. Nevertheless, when the concentration of $AgNO_3$ continued to increase (Fig. 4A(c-d)), the AgNPs were agglomerated with a non-uniform size

distribution, and the Raman intensity showed a considerable decrease. This phenomenon can be ascribed to the rapid formation of crystal nuclei caused by the high concentration of $AgNO_3$. This led to the aggregation of AgNPs, which hindered the contact between 4-MBA and the AgNPs, resulting in a weakened signal. [33] Therefore, 40 mM of $AgNO_3$ was chosen as the immersion concentration.

After incubation with the Si@AgNPs, the UV absorbance at 262 nm of the supernatant, corresponding to the complementary chain of the aptamer, was significantly reduced, indicating a decrease in the content of the complementary chain of the aptamer in the solution, the aptamer was successfully coupled to the Si@AgNPs by Ag-S bonds (Fig. S3).

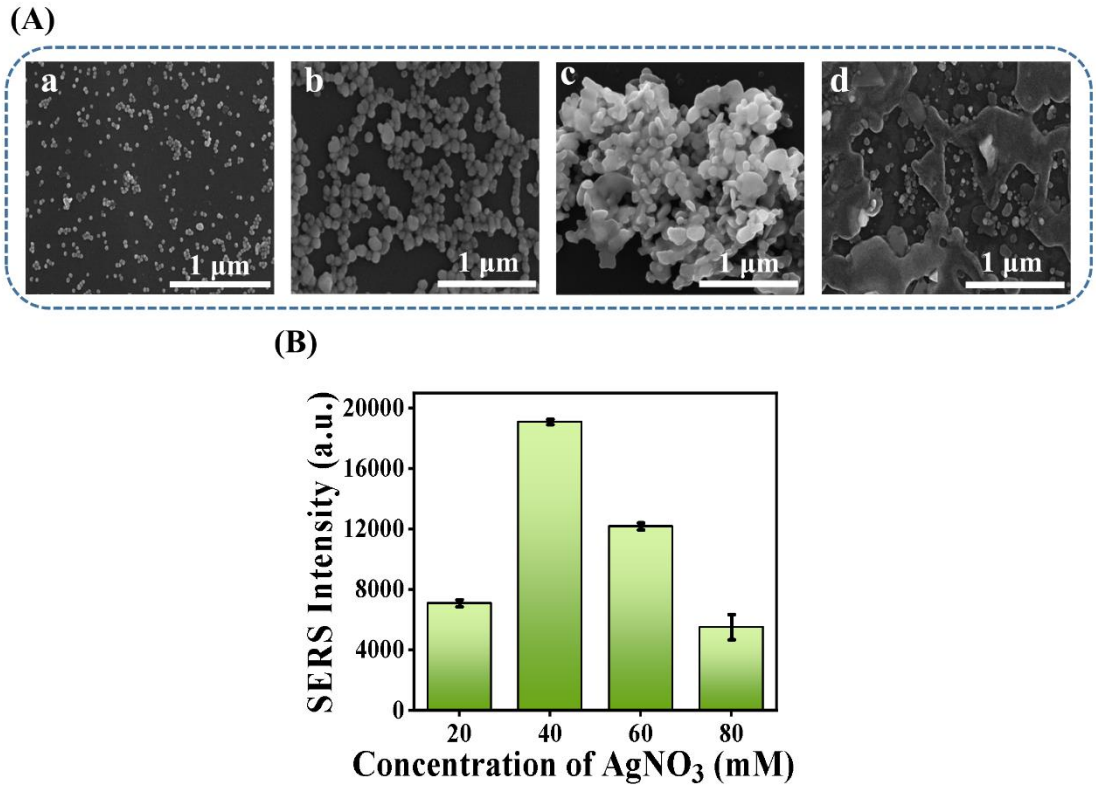

Fig. 4 (A) SEM images of Si@AgNPs substrates prepared with different concentrations of $AgNO_3$, (a) 20 mM, (b) 40 mM, (c) 60 mM, (d) 80 mM, (B) The effect

of $AgNO_3$ concentration on SERS intensity of SERS aptasensor.

3.4 Characterization and optimization of SERS aptasensor (Au^{MBA}@Ag NPs-Apt-cDNA-AgNPs@Si)

EDS was used to ensure the effective connection between the signal and the capture probes. In the element mapping image (Fig. 5A) and the Map sum spectrum (Fig. S4), the silicon wafer showed both Ag and Au elements, and the Au elements were uniformly distributed on the silicon wafer. In addition, the presence of element C can be attributed to the presence of low-boiling volatile organic compounds (VOCs) in the air, such as Acetic Acid (CH_3COOH), isoprene (C_5H_8), which adhered haphazardly to the sample's surface during the preparation and transportation. In addition, the silicon wafer did not display a Raman signal within the wavelength range of 600-1800 cm^{-1} and was therefore excluded in the subsequent analysis. The Raman signal of 10^{-6} M 4-MBA dropped on the Si@AgNPs was effectively enhanced by the LSPR effect of the Ag nanoparticles, and Si@AgNPs chip produced strong Raman signals belonging to 4-MBA after incubation with Au^{MBA}@Ag NPs, proving the formation of SERS aptasensors (Fig. 5B).

The optimal incubation time for the capture probe and the signal probe was determined by the intensity of 4-MBA at 1580 cm^{-1} (Fig. 5C). At shorter incubation times, the SERS intensity of the sensor was low. The limited binding of signal probes to the silicon substrate could account for this phenomenon. With the extended incubation time, the signal intensity initially escalated and subsequently declined because prolonged immersion will lead to the shedding of the signal probe. As a result,

the optimal incubation time was identified as 8 h.

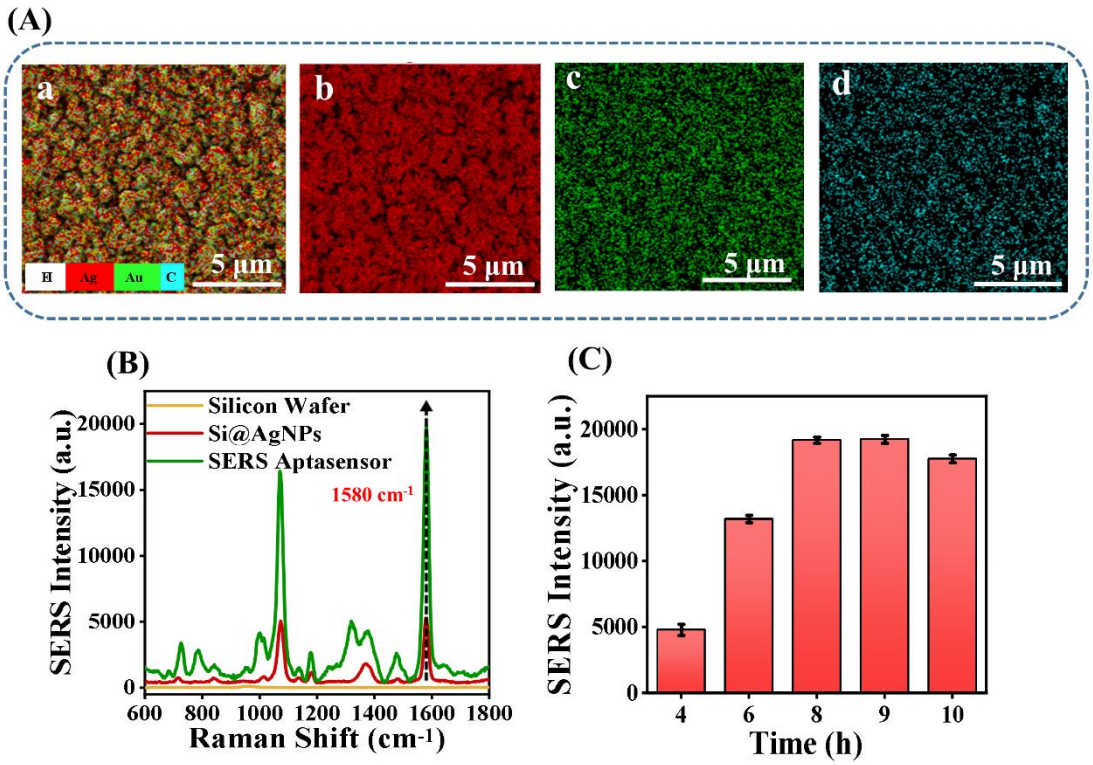

Fig. 5 (A) EDS elemental mapping image of SERS aptasensor, (a) Total elemental image, (b) Ag, (c) Au, (d) C, (B) Raman spectra of Silicon Wafer, Si@AgNPs, SERS aptasensor, (C) Optimization of incubation time of signal probe with capture probe.

3.5 Detection of AFB1 in standard solution and corn samples

3.5.1 AFB1 detection

Based on the optimal parameters for constructing the SERS aptasensor, the SERS intensity in the presence of AFB1 standard solutions with gradient concentrations was studied, The increase of AFB1 concentration led to a gradual decrease in the SERS intensity (Fig. 6A). The standard curve was plotted using the peak intensity at 1580 cm^{-1} and the lg value of AFB1 concentration (Fig. 6B). The linear correlation coefficient (R^2) for the standard curve at the concentration range of 0.05-20.0 ng/mL was 0.991

pointing to reasonable linearity.

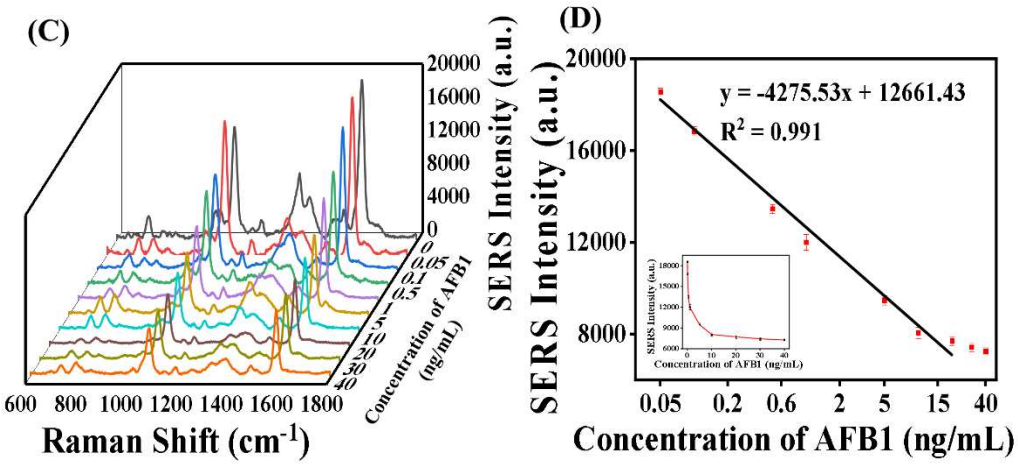

Fig. 6 (A) Raman spectra of SERS aptasensor corresponding to the changes of AFB1 concentration, (B) tandard curve of SERS intensity of SERS aptasensor at 1580 cm^{-1}.

The calculation method of limit of detection (LOD) refered to previous literature, [34] and the formula is as follows:

$$LOD = 10^{\frac{y0-3\sigma-b}{k}} \quad (1)$$

y_0 = The Raman peak intensity of the blank sample, σ = The SD value of the blank sample's peak, b = The intercept of the standard curve, k = the slope of the standard curve.

The calculated LOD was 0.039 ng/mL, significantly below the minimum limit standard set by China. In addition, this scheme had better sensitivity compared with the already reported AFB1 detection methods (Table 1).

Table 1 Comparison of different detection methods.

Method	Detection method	Linear detection range	LOD (ng/mL)	Reference

comparison		(ng/mL)		
	Fluorescent aptasensor	0-3	0.25	35
	Colorimetric aptasensor	0.2-8	0.08	36
	Molecularly imprinted polymer	20-100	20	37
	Lable-free electrochemistry sensor	10-250	3.19	38
	Label-free SERS sensor	5-1000	1.8	39
	SERS aptasensor	0.05-20	0.039	This Work

3.5.2 AFB1 detection in corn flour and corn oil samples

Corn products were tested using the SERS aptasensor and the HPLC method. The concentration of AFB1 in the real sample with the Raman detection method was calculated according to the established SERS standard curve, the calculation was carried out according to:

$$X = \frac{\rho \times V}{m} \quad (2)$$

ρ = the AFB1 concentration in the sample solution corresponding to the signal intensity of the standard curve (ng/mL), V = the concluding volume (mL), m = sample weight (g)).

SERS spectra of various samples and peak intensity at 1580 cm^{-1} are shown in Fig. S5. HPLC was employed as the standard method to verify the accuracy of the SERS detection method, with the standard curve and representative outcomes are shown in Fig. S6-S7. The recovery rate of the sample was between 92.77% and 110.13%, with

an RSD (n = 3) of 1.29% to 4.24%, closely matching the detection results of HPLC (Table 2). Therefore, the aptasensor demonstrates good practicability and holds promise for precise and sensitive detection of AFB1 in corn.

Table 2 Detection results of AFB1 in real samples by SERS aptasensor and HPLC methods

	Samples	Spiked (μg/kg)	SERS			HPLC	
			Detected (μg/kg)	Recovery (%)	RSD (%,n=3)	Detected (μg/kg）	Recovery (%)
Corn samples detection	Naturally contaminated cornmeal	/	9.008	92.77	1.5	9.712	/
		/	2.381	93.39	2.66	2.555	/
	Spiked cornmeal	10	10.322	103.22	4.07	10.053	100.53
		5	5.355	107.10	1.49	4.592	91.84
	Spiked corn oil	10	11.013	110.13	4.24	10.769	107.69
		2.5	2.381	93.39	2.66	2.516	100.64

3.6 Selectivity, uniformity, stability of sensors

The specificity of the system was evaluated by measuring the SERS intensity after incubation with AFB1, OTA, ZEN, DON, FB1, OTA-AFB1, ZEN-AFB1, DON-AFB1, and FB1-AFB1 (Fig. 7A). Although the concentration of the interfering toxins (100 ng/mL) was 100 times that of AFB1 (1 ng/mL), it did not cause any noticeable change in the Raman signal. Similar to the case when AFB1 was added alone, the addition of mixtures of interfering toxins with AFB1 resulted in a significant decrease in the system's signal, indicating that the aptasensor exhibits good selectivity for AFB1.

Uniformity is also an important evaluation index for assessing the quality of an experimental protocol. The Raman spectra at 16 random points were collected after the sensor was incubated with 0.1 ng/mL AFB1 standard solution (Fig. S8). The relative standard deviation (RSD) of the 1580 cm^{-1} peak was approximately 6.38% (Fig. 7B), indicating the relatively good uniformity of the system. The aptasensor stored at 4℃ showed consistent Raman signal intensity over four weeks, making it a stable platform for AFB1 detection (Fig. 7C), which was consistent with the description that silicon wafer can be used as the bearing substrate of stable SERS reinforced materials.

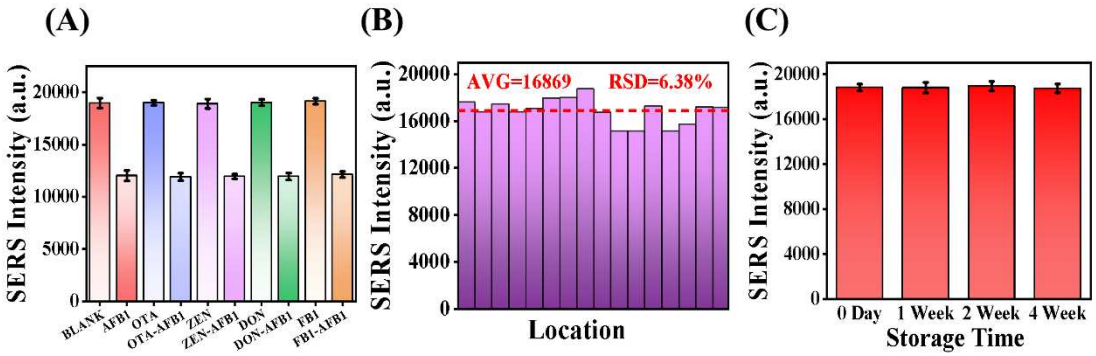

Fig. 7 (A) Selective evaluation of aptasensor, (B) SERS intensity at 1580 cm^{-1} collected from 16 random points of SERS aptasensor after incubation with 0.1 ng/mL AFB1, (C) Raman signals changes of SERS aptasensor with time.

4. Conclusion

In this study, Au^{MBA}@Ag NPs-Apt and Si@AgNPs-cDNA were prepared as signal probes and capture probes, respectively, and their synthesis parameters were optimized. Subsequently, the probes were combined to establish a sensitive SERS aptasensor with an abundant number of hot spots. AFB1 was bound to the aptamer prior to cDNA since

aptamers showed a high affinity to it, thus the signal probe dissociated from the capture probe. This disassociation led to a reduction in SERS intensity corresponding to the concentration of AFB1. Under optimum conditions, the linear detection range of the scheme was 0.05-20 ng/mL, with a LOD of 0.039 ng/mL, well below the national standard limit. The recovery rate for the detection of corn flour and oil fluctuated from 92.77% to 110.13%, which verified the accuracy of the results and proves the practical applications of the aptasensor. In addition, the strategy showed good stability and high specificity. In summary, this scheme conveys an intriguing possibility for application in the detection of AFB1. Nevertheless, reducing the incubation time between the aptasensor and the target analyte to better achieve on-site detection still requires exploration and improvement. For instance, utilizing the exponential enrichment (P-SELEX) strategy, we can attempt to find aptamers with stronger affinity by comparing screening steps with and without target introduction.

Author contributions

Zhiming Guo: Conceptualization, Supervision, Funding acquisition, Project administration. **Xuan Fu**: Investigation, Methodology, Roles/Writing - original draft. **Ruiyun Zhou**: Methodology, Resources, Visualization. **Heera Jayan**: Data curation, Investigation, Validation. **Yang Zhang**: Methodology, Validation, Visualization. **Shanshan Xue**: Validation, Visualization. **Hesham R. El-Seedi**: Writing – review & editing. **Nicholas J. Watson**: Writing – review & editing. **Xiaobo Zou**: Resources, Supervision. **Megan Povey**: Writing – review & editing.

Conflicts of interests

There are no conflicts to declare.

Acknowledgements

This research was funded by the National Key R&D Program of China (2023YFE0107100), National Natural Science Foundation of China (31972151), the Outstanding Young Teachers of Blue Project in Jiangsu province, Key R&D Project of Jiangsu Province (BE2022363), Jiangsu Agriculture Science and Technology Innovation Fund (CX(22)3069).

References

1 T. Jiao, W. Ahmad, J. Zhu, M. M. Hassan, J. Wang, Y. Rong, Z. Guo, H. Li, Z. Ding, C. Lv and Q. Chen, *Sensors and Actuators B: Chemical*, 2021, **331**, 129424.

2 J. Wang, Q. Chen, Y. Jin, X. Zhang, L. He, W. Zhang and Y. Chen, *Analtica Chimica Acta*, 2020, **1128**, 184-192.

3 W. Zhang, S. Tang, Y. Jin, C. Yang, L. He, J. Wang and Y. Chen, *Journal of Hazardous Materials*, 2020, **393**, 122348.

4 A. Zhu, T. Jiao, S. Ali, Y. Xu, Q. Ouyang and Q. Chen, *Food Chemistry*, 2022, **391**, 133277.

5 P. Yogendrarajah, F. Devlieghere, E. Njumbe Ediage, L. Jacxsens, B. De Meulenaer and S. De Saeger, *Food Microbiology*, 2015, **52**, 185-196.

6 A. E. Urusov, A. V. Petrakova, M. V. Vozniak, A. V. Zherdev and B. B. Dzantiev, *Sensors (Basel)*, 2014, **14**, 21843-21857.

7. Z. Guo, Y. Zheng, L. Yin, S. Xue, L. Ma, R. Zhou, H. R. El-Seedi, Y. Zhang, N. Yosri, H. Jayan and X. Zou, *Sensors and Actuators B: Chemical*, 2024, **404**, 135303.

7 J. Wei, Y. He, Z. Song, I. M. Khan, Z. Wang, C. Jiang and X. Ma, *Food Control*, 2024, **156**, 110112.

8 A. Li, L. Tang, D. Song, S. Song, W. Ma, L. Xu, H. Kuang, X. Wu, L. Liu, X. Chen and C. Xu, *Nanoscale*, 2016, **8**, 1873-1878.

9 A. Hussain, D. W. Sun and H. Pu, *Food Chemistry*, 2020, **317**, 126429.

10 Z. Guo, X. Wu, H. Jayan, L. Yin, S. Xue, H. R. El-Seedi and X. Zou, *Food Chemistry*,

2024, **434**, 137469.

11 Y. Zhao, Y. Yang, Y. Luo, X. Yang, M. Li and Q. Song, *ACS Applied Materials Interfaces*, 2015, **7**, 21780-21786.

12 J. Wang, Z. Luo and X. Lin, *Food Chemistry*, 2023, **402**, 134433.

13 X. Ma, B. Shao and Z. Wang, *Analytica Chimica Acta*, 2021, **1188**, 339189.

14 S.-J. Ding and J. Zhu, *Applied Surface Science*, 2015, **357**, 487-492.

16. L. Yin, J. Cai, L. Ma, T. You, M. Arslan, H. Jayan, X. Zou and Y. Gong, *Food Chemistry*, 2024, **446**, 138817.

15 X. Li, X. Lin, G. Fang, H. Dong, J. Li, S. Cong, L. Wang and S. Yang, *Journal of Colloid and Interface Science*, 2022, **620**, 388-398.

16 D. Lin, Z. Wu, S. Li, W. Zhao, C. Ma, J. Wang, Z. Jiang, Z. Zhong, Y. Zheng and X. Yang, *ACS Nano*, 2017, **11**, 1478-1487.

17 S. Verma, V. S. Bitra, R. Singh and B. T. Rao, *Materials Chemistry and Physics*, 2023, **306**, 128058.

18 J. Wu, Y. Du, C. Wang, S. Bai, T. Zhang, T. Chen and A. Hu, *Applied Surface Science*, 2019, **494**, 583-590.

21. G. Xu, C. Wang, H. Yu, Y. Li, Q. Zhao, X. Zhou, C. Li and M. Liu, *Nucleic Acids Research*, 2023, **51**, 7666-7674.

20 L. Yin, T. You, H. R. El-Seedi, I. M. El-Garawani, Z. Guo, X. Zou and J. Cai, *Food Chemistry*, 2022, **396**, 133707.

21 X. Ma, S. Xu, L. Li and Z. Wang, *Spectrochimoca Acta Part A-Molecular and*

Biomolecular Spectroscopy, 2023, **284**, 121757.

22 B. Fan, Y. Wang, Z. Li, D. Xun, J. Dong, X. Zhao, X. Fan and Y. Wang, *Talanta*, 2022, **238**, 122988.

23 B. Yuan, X. Jiang, C. Yao, M. Bao, J. Liu, Y. Dou, Y. Xu, Y. He, K. Yang and Y. Ma, *Analytica Chimica Acta*, 2017, **955**, 98-107.

24 Y. Chen, W. Cheng, Y. Yang, D. Wu, Y. Zhang and X. Tang, *Sensors and Actuators B: Chemical*, 2023, **393**, 134329.

25 Z. Guo, L. Gao, S. Jiang, H. R. El-Seedi, I. M. El-Garawani and X. Zou, *Journal of Food Composition and Analysis*, 2023, **115**, 104985.

26 A. Zhu, T. Jiao, S. Ali, Y. Xu, Q. Ouyang and Q. Chen, *Analytical Chemistry*, 2021, **93**, 9788-9796.

27 K. Wang, D. W. Sun, H. Pu and Q. Wei, *Talanta*, 2019, **195**, 506-515.

28 L. Yin, T. You, M. Arslan, H. R. El-Seedi, Z. Guo, X. Zou and J. Cai, *Food Chemistry*, 2023, **429**, 136834.

29 K. V. Serebrennikova, O. D. Hendrickson, E. A. Zvereva, D. S. Popravko, A. V. Zherdev, C. Xu and B. B. Dzantiev, Biosensors (Basel), 2020, **10**, 198.

30 H. Zheng, D. Ni, Z. Yu and P. Liang, *Food Chemistry*, 2017, **217**, 511-516.

33. X. Gao, Y. Liu, J. Wei, Z. Wang and X. Ma, *Spectrochimica Acta Part A: Molecular and Biomolecular Spectroscopy*, 2024, **315**, 124268.

31 L. Ma, Q. Xu, L. Yin, C. Zou, W. Wu, C. Wang, R. Zhou, Z. Guo and J. Cai, *Microchemical Journal*, 2024, **204**, 111021.

32 Y. Jia, F. Wu, P. Liu, G. Zhou, B. Yu, X. Lou and F. Xia, *Talanta*, 2019, 198, 71-77.

33 L. Lu, R. Yu and L. Zhang, *Food Chemistry*, 2023, **421**, 136205.

34 T. Sergeyeva, D. Yarynka, E. Piletska, R. Linnik, O. Zaporozhets, O. Brovko, S. Piletsky and A. El'skaya, *Talanta*, 2019, **201**, 204-210..

35 J. Qian, Y. Liu, H. Cui, H. Yang, M. Hussain, K. Wang, J. Wei, L. Long, L. Ding and C. Wang, *Analytica Chimica Acta*, 2023, **1282**.

36 J. Li, H. Yan, X. Tan, Z. Lu and H. Han, *Analtical Chemistry*, 2019, **91**, 3885-3892.